On the Reaction Mechanism of MCrAlY Alloys with Oxide–Sulfate Deposits at 1100 °C

Thomas Gheno, Brian Gleeson

To cite this version:

Thomas Gheno, Brian Gleeson. On the Reaction Mechanism of MCrAlY Alloys with Oxide–Sulfate Deposits at 1100 °C. Oxidation of Metals, 2016, 86 (5-6), pp.385-406. ⟨10.1007/s11085-016-9649-5⟩. ⟨hal-01956143⟩

On the Reaction Mechanism of MCrAlY Alloys with Oxide–Sulfate Deposits at 1100 °C

Thomas Gheno* and Brian Gleeson
Department of Mechanical Engineering and Materials Science,
University of Pittsburgh, Pittsburgh PA 15261, USA
Email: thomas.gheno at gmail; bgleeson at pitt.edu

This is a post-peer-review, pre-copyedit version of an article published in
Oxidation of Metals. The final version is available online at:
https://doi.org/10.1007/s11085-016-9649-5

Abstract The corrosion of γ–(Ni,Co) + β–(Ni,Co)Al NiCoCrAlY alloys exposed to CaO-rich, Na_2SO_4-containing deposits in air and CO_2–H_2O–O_2 at 1100 °C was studied with a focus on the mechanisms governing the accelerated attack of γ-rich compositions. Internal oxidation of Al resulted from the breakdown of an initially formed Al_2O_3 scale, due to its reaction with the deposit. Compared to deposit-free conditions, this scale exhibited: (i) a delayed Al_2O_3 structure transition from metastable θ to stable α; (ii) finer grains; (iii) a reduced adherence to the metal, to the extent that a gap developed at the metal/oxide interface; and (iv) significant permeability to S, as well as N during air exposures. The occurrence of sulfidation in S-free gases reflected the establishment of an elevated S activity under the molten Na_2SO_4, due to the locally reduced p_{O_2}. The factors affecting the Al_2O_3-scale microstructure were examined, as well as the associated consequences on Al consumption and on the transition to internal oxidation. The roles of alloy and gas compositions in the identified mechanisms were also discussed.

Keywords MCrAlY coatings; Al_2O_3 scale; Selective oxidation; Silicate deposits

1 Introduction

High-temperature structural materials are primarily designed for optimal mechanical properties, and often require coatings to withstand corrosion in the chemically harsh environments they are exposed to. In particular, MCrAlY coatings (M = Ni, Co, or both), based on the fcc-A1 solid solution γ-(Ni,Co) and the B2 compound β-(Ni,Co)Al, are used to protect Ni-base materials in aero, marine and land-based power generation turbines [1, 2]. Environmental factors affecting their corrosion resistance include the presence of oxidants in gaseous form (e.g., O_2, CO_2, H_2O, and SO_2) or as condensed phases, such as silicates or sulfates.

The oxidation behavior of MCrAlY coatings in deposit-free conditions, and specifically the mechanisms governing the establishment of a protective Al_2O_3 scale, are relatively well documented (e.g., Refs. [3–7]). A considerable body of work has been devoted to the effects of H_2O on the oxidation of Al_2O_3-forming alloys (see reviews in Refs. [8–10]). Although some aspects are system-dependent, it is generally found that H_2O accelerates Al_2O_3 growth and enhances scale cracking and spallation. Much less information is available regarding the role of CO_2 or SO_2 in

---

[*] now at DEN-Service de la Corrosion et du Comportement des Matériaux dans leur Environnement, CEA, Université Paris-Saclay, 91191 Gif-sur-Yvette, France

these systems. Recent investigations on Fe-base [11] and Ni-base [12] Al_2O_3-forming alloys in CO_2–H_2O found no significant effect of CO_2. This is in contrast with Cr_2O_3-formers, which are subject to carburization in CO_2, indicating that Al_2O_3 is a much better barrier to carbon than Cr_2O_3 is [9].

Research on deposit-induced degradation of Al_2O_3-forming systems has mostly concerned hot corrosion, a form of accelerated corrosion by molten sulfates which can be particularly severe at 700–900 °C [13–18]. Fly ash deposits relevant to gas turbines mainly contain some combination of SiO_2, Al_2O_3, CaO, MgO, and Fe_2O_3 [19], with additions of Na, K, and S [20]. The reaction of these constituents with bond coat materials has received little attention because the oxide melting points far exceed the operating temperature of any metal component. Yet liquid phases may form at relatively low temperatures upon reaction of SiO_2 with the alkali metal oxides (the lowest eutectic points in the Na_2O–SiO_2 and K_2O–SiO_2 systems are at 794 and 743 °C, respectively [21]), or of CaO with thermally grown oxides such as Cr_2O_3. The lowest eutectic point in the CaO–Cr_2O_3 system is not known with precision (conflicting values of 1022 °C [22] and 1061 °C [23] are reported), but catastrophic corrosion of Ni–Cr alloys due to liquid Ca chromate formation has been observed down to 1000 °C [24].

In recent papers, we studied the reactivity of cast γ–β NiCoCrAlY alloys with CaO [25] and various oxide–sulfate deposits in S-free gases at 1100 °C [26,27]. Alloys with a high Cr concentration and high γ fraction, which have optimal hot corrosion resistance, were found to be particularly susceptible to accelerated corrosion when exposed to CaO-rich, Na_2SO_4-containing deposits. In addition to liquid Ca chromate formation, two modes of degradation were identified, which involved Al_2O_3 dissolution in molten Na silicate and solid-state Al_2O_3 reaction with CaO to form Ca aluminate. Both led to enhanced Al consumption, destabilizing the external Al_2O_3 and promoting internal oxidation. In the present paper, we study the reaction mechanism of NiCoCrAlY alloys exposed to CaO-rich, Na_2SO_4-containing deposits at 1100 °C, with particular attention to the onset of non-selective oxidation. The effects of the deposit constituents on Al_2O_3 formation are assessed based on microstructural characterization of scales grown with and without deposit.

2 Materials and experiments

Cast NiCoCrAlY alloys of nominal compositions given in Table 1 were used in this study. These included a β-rich composition with relatively high Al and low Cr, and six γ-rich alloys with 30 Co (all alloy compositions in at. %) and variations of Al and Cr (12/16 Al, 27/30/33 Cr). All alloys had 0.1 Y. Ingots were made by argon-arc melting, followed by drop casting into 10-mm diameter rods which were then homogenized in vacuum for 6 h at 1200 °C plus another 48 h at 1150 °C. All processing was conducted at the Materials Preparation Center of the Ames Laboratory [28]. Approximately 1-mm-thick specimens were cut from the heat-treated rods, ground using SiC paper to a P1200-grit finish, then degreased with detergent and ultrasonically cleaned in ethanol before exposure.

Microstructures were characterized after a further 50-h annealing at 1100 °C followed by air cooling. All alloys had a primary γ–β microstructure; volume fractions of β measured by image analysis using the ImageJ software [29] are included in Ta-

Table 1: Nominal composition of NiCoCrAlY alloys used in the present study (at. %). Volume fractions of β, f_β, were measured by image analysis after annealing at 1100 °C.

#	Elemental concentration (at. %)					f_β at 1100 °C
	Ni	Co	Cr	Al	Y	(vol. %)
UT2	42	19	15	24	0.1	57
UT3	31	30	27	12	0.1	13
UT4	28	30	30	12	0.1	16
UT5	25	30	33	12	0.1	18
UT6	27	30	27	16	0.1	34
UT7	24	30	30	16	0.1	40
UT8	21	30	33	16	0.1	42

ble 1. The alloys precipitated a small amount of yttrium-rich intermetallics (0.1 vol. %), and some also contained σ–CoCr (1, 2, and 22 vol. % in Ni–30Co–33Cr–12Al–0.1Y, Ni–30Co–30Cr–16Al–0.1Y, and Ni–30Co–33Cr–16Al–0.1Y, respectively).

Isothermal corrosion experiments were conducted at 1100 °C in flowing dry air ($<$ 1 ppm CO_2 and CO, $<$ 2 ppm H_2O), air–$20H_2O$, CO_2–$20H_2O$ and CO_2–$20H_2O$–$1.6O_2$ (vol. %), using a horizontal tube furnace. Gas flow rates were set to 100 ml/min, with a linear velocity of 2 mm/s at reaction temperature, and a total pressure slightly over 1 atm. To obtain a wet gas, the dry air, CO_2 or CO_2–O_2 was bubbled through demineralized water set at 62 °C, thereby producing a mixture with slightly more than the desired 0.2 atm H_2O. The excess water vapor was subsequently condensed by cooling the wet gas in a distillation column at 60 °C. Prior to a given experiment, the furnace was stabilized at 1100 °C with the specimens positioned in a cold zone of the reaction tube, and the gas was allowed to flow for 2 h. To start the experiment, the specimens were magnetically pushed in the hot zone.

The deposit compositions studied were SiO_2–$25Al_2O_3$–40CaO–$10Na_2SO_4$ and SiO_2–$20Al_2O_3$–33CaO–8MgO–$6Fe_2O_3$–$5Na_2SO_4$–$1K_2SO_4$ (wt. %). These were prepared by grinding laboratory-grade reagents using a mortar and pestle, and were given no heat treatment prior to corrosion testing. The powders were mixed with ethanol, and the resulting slurry was applied to one face of a given specimen using a dropper. The procedure was adjusted to produce approximately uniform 30 ± 5 mg/cm^2 deposits after evaporation of the ethanol. The experiments were all isothermal, with durations ranging from 5 min to 250 h, as indicated in the text. The same amount of deposit, 30 mg/cm^2, was applied once prior to each experiment, regardless of test duration.

After exposure, reaction products were examined by XRD, using a PANalytical Empyrean instrument with a Co radiation ($K_{\alpha 1}$ = 1.789 Å), and by photostimulated luminescence spectroscopy (PSLS), which allows γ, θ, and α polymorphs of Al_2O_3 to be distinguished [30], using a 633 nm HeNe laser in a Renishaw inVia Raman microscope. Surfaces were observed by optical microscopy with a Keyence VHX–600 and by SEM with a JEOL JSM–6510. In selected cases, thin foils were extracted from the specimen surface by focused ion beam (FIB) milling with a FEI

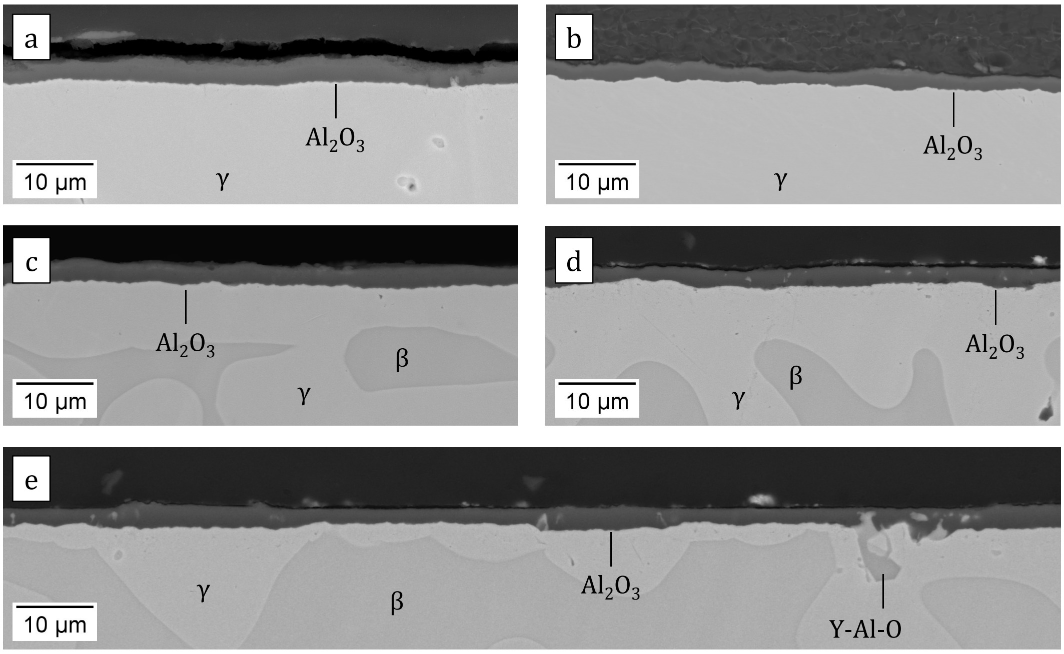

Figure 1: Oxide scales formed during exposure of (a), (b) Ni–30Co–27Cr–12Al–0.1Y, (c), (d) Ni–30Co–30Cr–16Al–0.1Y, and (e) Ni–19Co–15Cr–24Al–0.1Y in (a, c) dry air and (b, d, e) CO_2–$20H_2O$–$1.6O_2$, with no deposit, 50 h at 1100 °C.

Nova NanoLab 200, and characterized by transmission electron microscopy (TEM) on a Zeiss Libra 200FE and a JEOL JEM–2100F. In this case, deposits were washed off the surface prior to FIB milling. Polished cross-sections were prepared using conventional metallographic techniques. When a deposit was present, water-free cutting fluids and polishing suspensions were first used to retain any water-soluble products such as Na_2SO_4. Observations after short-term exposures showed that the sulfate had either reacted or evaporated, and so it was deemed appropriate to polish subsequent specimens in water-based media. The cross-sections were characterized by scanning electron microscopy (SEM) with a JEOL JSM–6510, and by EPMA with a JEOL JXA–8530F.

3 Results

3.1 Oxidation with no deposit

All alloys (Table 1) were oxidized 50 h in dry air, air–$20H_2O$, CO_2–$20H_2O$, and CO_2–$20H_2O$–$1.6O_2$ with no deposit. External Al_2O_3 scales formed in all cases; selected micrographs are shown in Fig. 1. Small regions of Cr, Co, and Ni oxides were occasionally found atop the scales, and the Al_2O_3 contained up to 1 at. % Cr in its outer part. The β-rich Ni–19Co–15Cr–24Al–0.1Y alloy also formed Y aluminate precipitates within the scale that locally extended into the alloy (Fig. 1e). These were less numerous if not absent in the γ-rich alloys. No particular effect of N_2, CO_2 or H_2O such as nitridation, carburization or enhanced spallation was observed in these isothermal exposures.

Scales formed on the alloys with 12 at. % Al, which had the lowest β fractions,

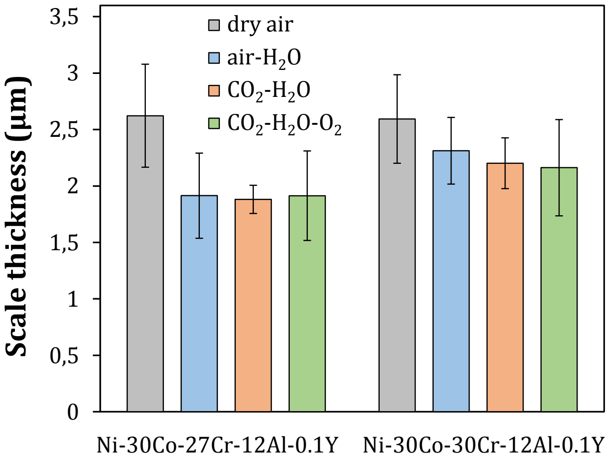

Figure 2: Average Al_2O_3 scale thickness measured on γ-rich alloys after exposure to various gases, 50 h at 1100 °C.

were relatively uniform. Average scale thicknesses were found to be consistently lower in the H_2O-containing gases than in dry air, as shown in Fig. 2. As the β fraction, f_β, increased, the effect of alloy microstructure became more prominent; specifically, the oxide located atop prior β domains was thinner than that formed on γ. For a simple mass balance reason, the depth of β dissolution decreased with increasing f_β, and therefore the effect of phase constitution on scale thickness was mostly visible on the alloy with highest f_β, as shown in Fig. 1e. Local thickness variations associated with alloy microstructure were less marked but also existed in the 16Al alloys. On average, these scales tended to be thinner than those formed on the 12Al alloys in dry air, and the difference between dry and H_2O-containing gases was less marked.

Two alloys, the β-rich Ni–19Co–15Cr–24Al–0.1Y and the γ-rich Ni–30Co–30Cr–12Al–0.1Y, were selected for shorter (5 and 20 min) oxidation in CO_2–$20H_2O$–$1.6O_2$. As shown in Fig. 3, different scale thicknesses on γ and β outlined the β-rich alloy microstructure. The scale grown on γ was thinner (see interference colors) and smooth, while that grown on β was thicker and granular. Both were Al_2O_3, as verified by SEM–EDS and XRD. Analysis by PSLS further showed that after 5 min, the oxide grown on β contained θ and α-Al_2O_3 in comparable proportions, while that formed on γ was fully transformed to α-Al_2O_3 (Fig. 4). After 20 min, the transformation was complete or nearly complete for the oxide grown on both alloy phases. Cross-sectional observation confirmed that the scale was significantly thicker on β (Fig. 5).

The scale grown on the γ-rich alloy was mostly thin Al_2O_3, identified as α by PSLS. The underlying γ–β microstructure was not apparent. Some Cr-rich oxide was present atop the Al_2O_3 with a surface coverage that varied with alloy grain orientation (Fig. 6a). This transient oxide was porous (Fig. 6b). Analysis by XRD showed that both Cr_2O_3 and spinel phases were present along with Al_2O_3 (Fig. 7). A TEM foil was prepared, which contained a zone of exclusive Al_2O_3 and a zone with some transient oxide, as shown in Fig. 8. When present as a single oxide, the Al_2O_3 had a typical two-layer microstructure: small equiaxed grains on the top,

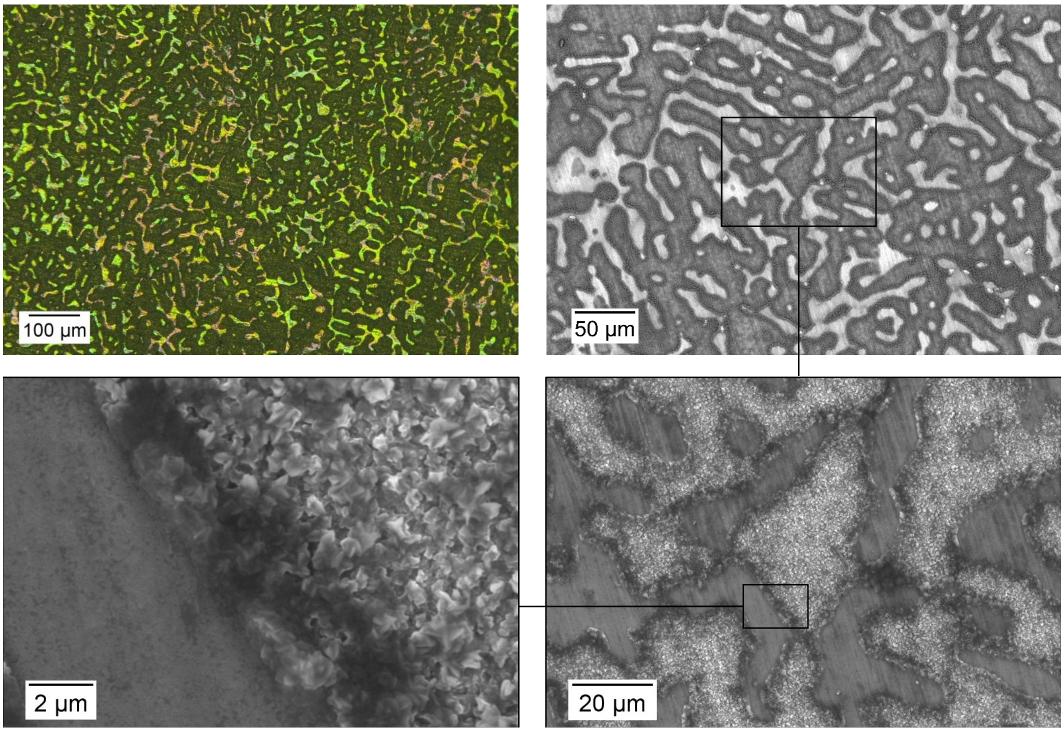

Figure 3: Surface micrographs of oxide grown on Ni–19Co–15Cr–24Al–0.1Y after 20 min in CO_2–$20H_2O$–$1.6O_2$ at 1100 °C, with no deposit. In top-left (light micrograph), the dark and neon phases are the oxides grown on β and γ, respectively. Top-right is an SEM–BSE image; at bottom (SEM–SE), the granular and smooth phases are the oxides grown on β and γ, respectively.

containing small amounts of Cr, Co, and Ni (1–6 at. %), and elongated grains at the bottom, with less than 1 at. % foreign species (Fig. 8b). When covered by transient oxide, the Al_2O_3 consisted of a single layer with large grains (Fig. 8d). The outer layer was a porous Co–Cr spinel, while small grains containing Al, Cr, and Co were present between the two layers.

3.2 Early-stage reaction with mixed oxide–sulfate deposit

In order to investigate the mechanism of deposit-induced accelerated attack, short exposures (20 min and 1 h) were conducted using selected alloys and one quaternary deposit: SiO_2–$25Al_2O_3$–40CaO–$10Na_2SO_4$ in CO_2–$20H_2O$–$1.6O_2$. The present section focuses on the 20-min reaction of the β-rich Ni–19Co–15Cr–24Al–0.1Y and the γ-rich Ni–30Co–30Cr–12Al–0.1Y.

Surface observations after the deposit was washed showed that the corrosion product had poor adherence to the alloys, as a significant part had spalled. The remaining surface oxide was either Al-rich or Cr-rich, with local variations. The underlying γ–β microstructure could not be distinguished on either alloy. Analysis of the surface oxides by PSLS showed that the Al-rich oxide was mostly α-Al_2O_3, but a significant amount of θ-Al_2O_3 remained, on both alloys. An example of a spectrum recorded on Ni–19Co–15Cr–24Al–0.1Y is included in Fig. 4.

Cross-sectional observations showed that the β-rich alloy mostly formed an ex-

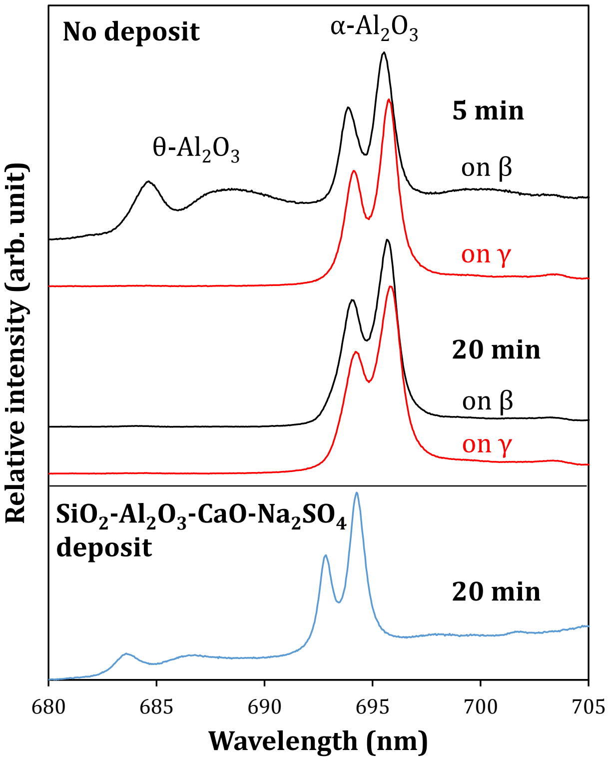

Figure 4: PSLS spectra recorded on the surface of Ni–19Co–15Cr–24Al–0.1Y reacted in CO_2–$20H_2O$–$1.6O_2$ at 1100 °C, with and without a SiO_2–$25Al_2O_3$–40CaO–$10Na_2SO_4$ deposit. Note that θ-Al_2O_3 luminescence is 10–12 times weaker than that of α-Al_2O_3 [30]. The proportions of θ and α varied on the specimen surfaces; the spectra included here are representative of $\sim$ 10 spectra recorded for each phase on each specimen. With the deposit, the underlying γ–β microstructure could not be identified from the surface: the spectra were recorded at random locations.

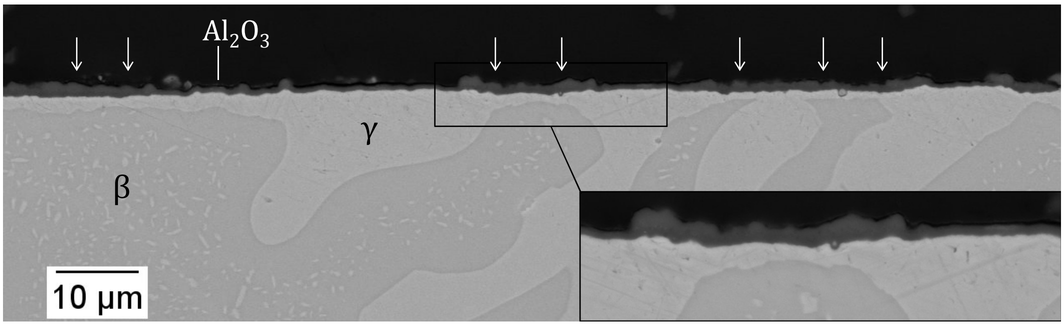

Figure 5: Cross-sectional view of Al_2O_3 scale grown on Ni–19Co–15Cr–24Al–0.1Y after 20 min in CO_2–$20H_2O$–$1.6O_2$ at 1100 °C, with no deposit. The scale is thicker above prior β regions (white arrows), where a thin band of γ has formed between the scale and the underlying β due to Al consumption.

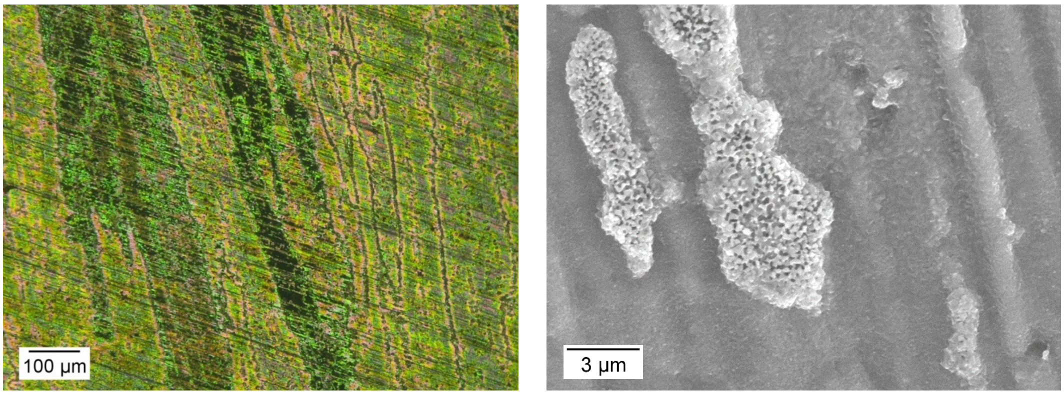

Figure 6: Surface micrographs of surface oxide grown on Ni–30Co–30Cr–12Al–0.1Y after 20 min in CO_2–$20H_2O$–$1.6O_2$ at 1100 °C, with no deposit. In the light image (left), Al_2O_3 appears neon, while Cr-rich oxide appears black. In the SEM image (right), Al_2O_3 appears dark-gray, while Cr-rich oxide appears light-gray.

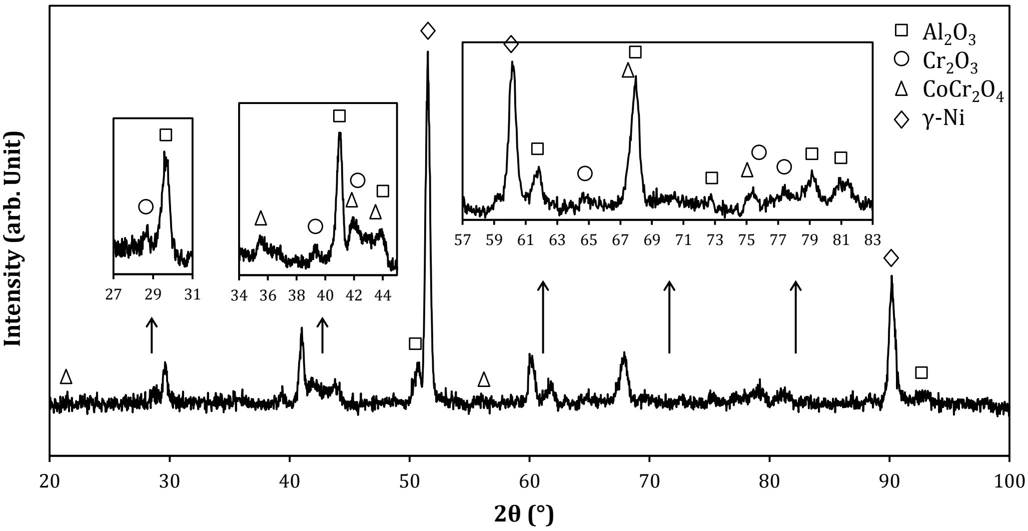

Figure 7: XRD patterns of oxide grown on Ni–30Co–30Cr–12Al–0.1Y after 20 min in CO_2–$20H_2O$–$1.6O_2$ at 1100 °C, with no deposit. Co radiation, grazing angle ($\Omega = 0.5°$).

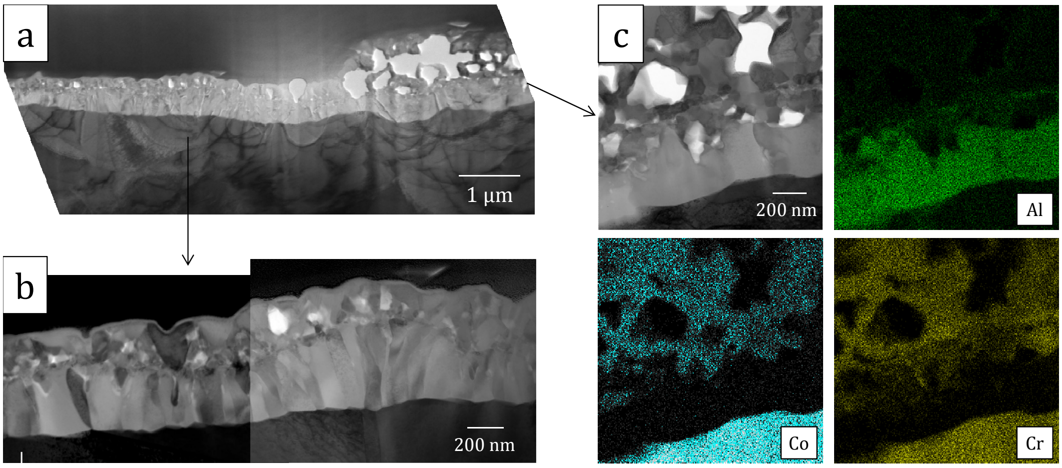

Figure 8: TEM observations of oxide grown on Ni–30Co–30Cr–12Al–0.1Y after 20 min in CO_2–20H_2O–1.6O_2 at 1100 °C, with no deposit. (a) overall bright field (BF) view; (b) BF view of Al_2O_3 scale; (c) STEM-BF view and EDS maps of region containing transient oxides and Al_2O_3 layer. Note that FIB milling amplified the existing porosity.

ternal Al_2O_3 scale, with a few isolated zones where Al_2O_3 intrusions less than 1-µm deep had grown into the alloy. By contrast, a transition to internal Al_2O_3 growth, although localized in nature, was consistently observed on the γ-rich alloy. Varying degrees of degradation were observed along the specimen cross-section. Figure 9 shows the EPMA maps of a region in the earliest stage of the transition, where small but numerous Al_2O_3 intrusions developed from the scale inward. An external Cr-rich oxide layer that included small amounts of Ni and Co, denoted Cr_2O_3, formed above the Al_2O_3. Aluminosilicates containing Ca and Na were present above the Cr_2O_3. Remarkably, S-rich zones were detected near the Al_2O_3 layer. A micrograph representative of the morphologies observed along the cross-section is shown in Fig. 10, where regions of apparently intact Al_2O_3 are seen side-by-side with Al_2O_3 intrusions and regions of internal Al_2O_3/external Cr_2O_3. Some degree of porosity was consistently observed at the base of the scale where the intrusions initiated.

Detailed characterization of the Ni–30Co–30Cr–12Al–0.1Y specimen was conducted by FIB and TEM. Searching for regions of interest by FIB milling confirmed that porosity was always present in the early stage of the external/internal Al_2O_3 transition. Figure 11 shows the TEM analysis of the scale at a stage where intrusions have not quite yet formed. In fact, the scale was separated from the alloy by a gap, and only connected in places by bridging grains. The scale was remarkably different in its microstructure from that grown in the absence of a deposit (compare with Fig. 8). In particular, the oxide grains were much finer, and no columnar zone was present. Analysis by EDS (Fig. 11b) showed that the scale contained a Ca aluminosilicate layer, a mixed Al–Cr oxide layer, and Al_2O_3 (from top to bottom). While most bridging grains across the alloy-scale gap were Al_2O_3, some were deduced to be Cr sulfide. Particles of the latter were also found within the scale and at the metal surface. Figure 12 shows the corrosion product in a more advanced stage of the transition, with a more variable and complex microstructure. Alumina intrusions developed inward and fine-grained Cr_2O_3 locally replaced Al_2O_3 as the external layer. Pores were constantly present throughout the corrosion product, in-

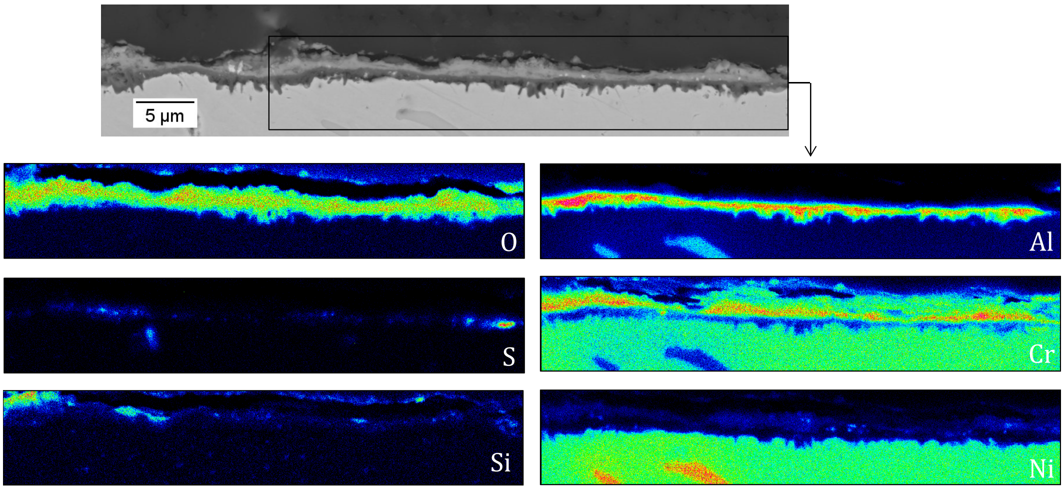

Figure 9: SEM view and WDS maps of corrosion product formed in the early stage of accelerated degradation on Ni–30Co–30Cr–12Al–0.1Y after 20-min exposure to SiO_2–25Al_2O_3–40CaO–10Na_2SO_4 deposit in CO_2–20H_2O–1.6O_2 at 1100 °C.

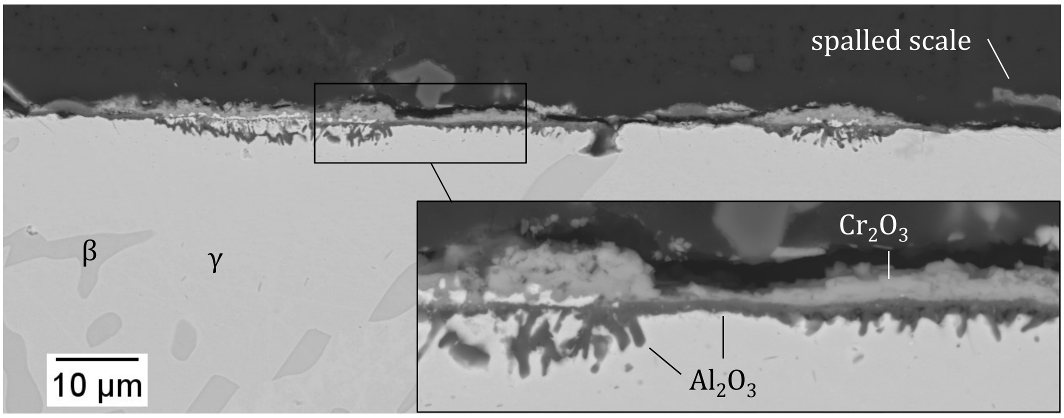

Figure 10: SEM cross-section of Ni–30Co–30Cr–12Al–0.1Y after 20-min exposure to SiO_2–25Al_2O_3–40CaO–10Na_2SO_4 deposit in CO_2–20H_2O–1.6O_2 at 1100 °C. Local variations in the reaction morphology reflect successive stages of the reaction process.

cluding within the Cr_2O_3. Analysis by EDS (Fig. 12b) showed that an Al_2O_3 layer was still present locally at the metal surface, while the sides of a large pore were lined with Cr-rich oxide and some mixed Cr–Ni sulfide. On the scale surface was a silicate layer that contained Ca and Al.

3.3 Effect of atmosphere and evolution of the reaction morphology

Potential effects of the gas atmosphere were studied using a SiO_2–20Al_2O_3–33CaO–8MgO–6Fe_2O_3–5Na_2SO_4–1K_2SO_4 deposit. This composition can be classified as class C fly ash, and has similar effects as the SiO_2–25Al_2O_3–40CaO–10Na_2SO_4 mixture [26]. The γ-rich alloy Ni–30Co–27Cr–12Al–0.1Y was exposed to SiO_2–20Al_2O_3–33CaO–8MgO–6Fe_2O_3–5Na_2SO_4–1K_2SO_4 for 1 h in dry air, CO_2–20H_2O–1.6O_2, and CO_2–20H_2O. The equilibrium p_{O_2} in the latter gas mixture is calculated to be

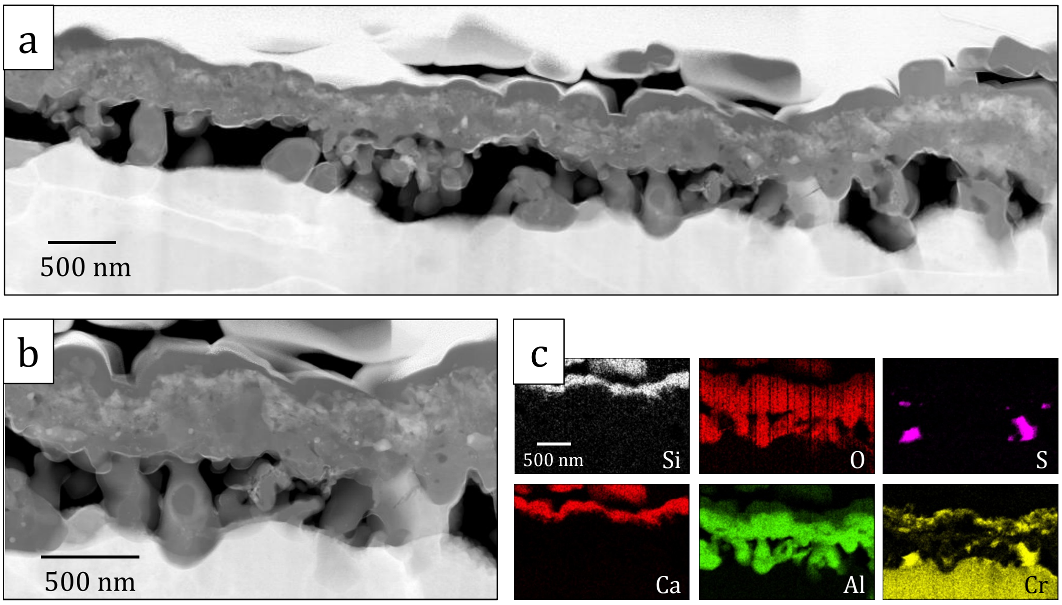

Figure 11: TEM analysis of oxide scale formed on Ni–30Co–30Cr–12Al–0.1Y after 20-min exposure to SiO_2–$25Al_2O_3$–40CaO–$10Na_2SO_4$ deposit in CO_2–$20H_2O$–$1.6O_2$ at 1100 °C, in region where accelerated corrosion has not started. (a) STEM high angle annular dark field (HAADF) overview; (b) STEM-HAADF view of oxide scale and alloy-scale interfacial gap, and (c) corresponding EDS maps.

4.3×10^{-5} atm from available thermodynamic data [31]. No particular effect of the p_{O_2} or of the presence of CO_2 or H_2O was found. The same reaction morphology was observed in all cases, and it was also equivalent to that obtained after 20-min reaction with the quaternary deposit (see previous section). Figure 13 presents the EPMA maps recorded after 1 h in CO_2–$20H_2O$–$1.6O_2$. While the alloy was still partially covered by an external Al_2O_3 scale, in other regions, Al_2O_3 intrusions penetrated about 5 µm into the metal. These partially joined at the reaction front to form a subsurface Al_2O_3 layer. Sulfur enrichments were found at locations corresponding to the initially formed Al_2O_3 and to the intrusions. A Cr_2O_3 layer covered by a mixed silicate was present above the internal oxidation zone.

Figure 14 shows the reaction products obtained after 1, 50, and 250 h exposures in dry air, with the same alloy and deposit. The presence of N_2 caused internal nitridation of Al, but this did not apparently make the deposit-induced degradation worse. The reaction morphology observed early was maintained over time. From 1 to 50 h, internal oxidation progressed, the nitrides coarsened and penetrated deeper, and a nitride-free zone developed below the scale, where Al depletion was most severe. Yet the new Al_2O_3 layer formed at the base of the internal oxides provided effective repassivation, since the reaction product did not significantly thicken between 50 and 250 h. It is noted that nitridation was observed throughout the cross-sections, even in zones where an apparently intact Al_2O_3 scale was present and no intrusions had formed, which still existed after 250 h. No nitridation occurred when the same alloy was oxidized in air with no deposit.

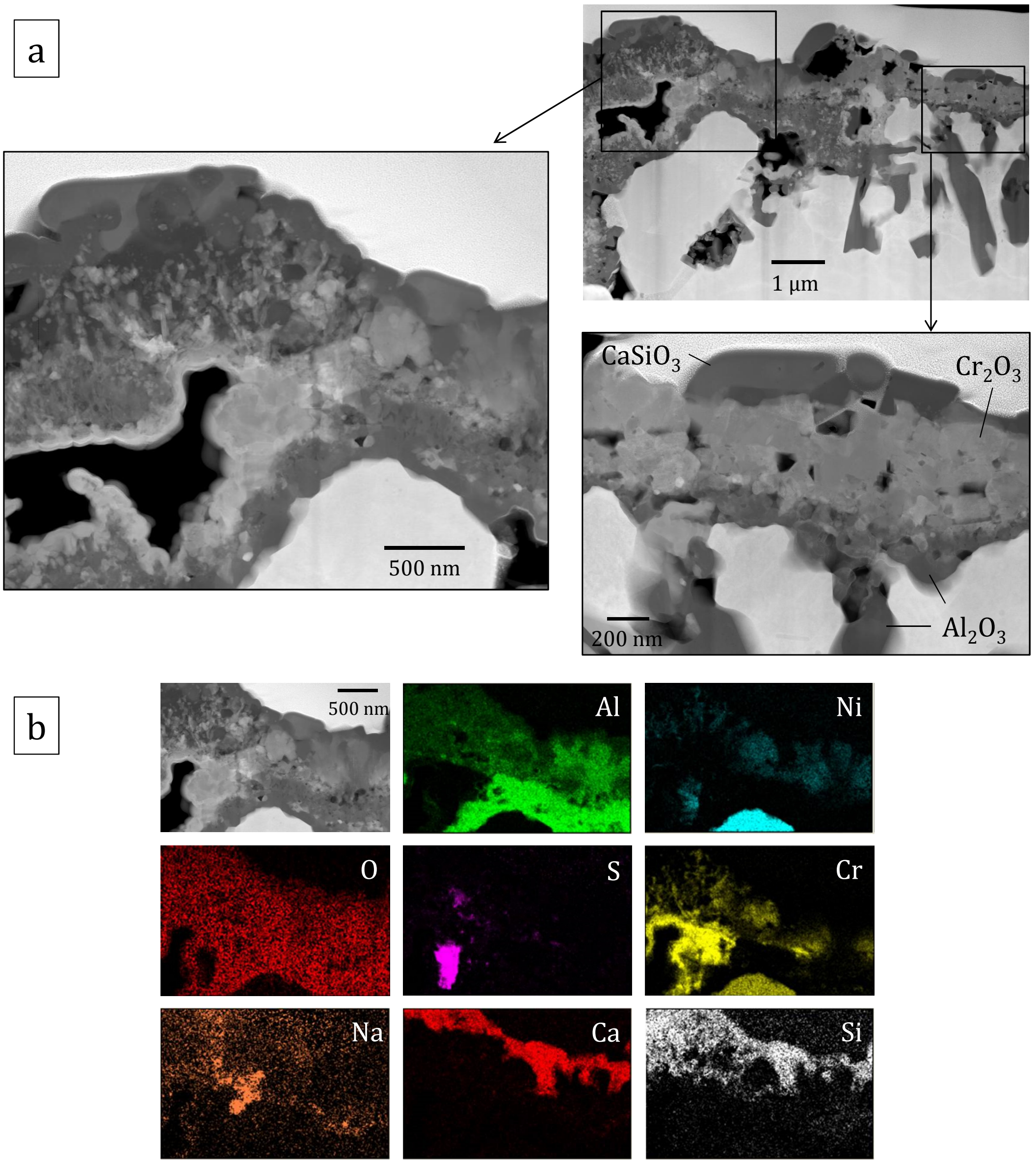

Figure 12: TEM analysis of corrosion product formed on Ni–30Co–30Cr–12Al–0.1Y after 20-min exposure to SiO_2–25Al_2O_3–40CaO–10Na_2SO_4 deposit in CO_2–20H_2O–1.6O_2 at 1100 °C, in region of accelerated corrosion. The scale contains Al_2O_3 and Cr_2O_3 layers surmounted by mixed silicates, and Al_2O_3 fingers grow internally. (a) STEM-HAADF images; (b) EDS maps.

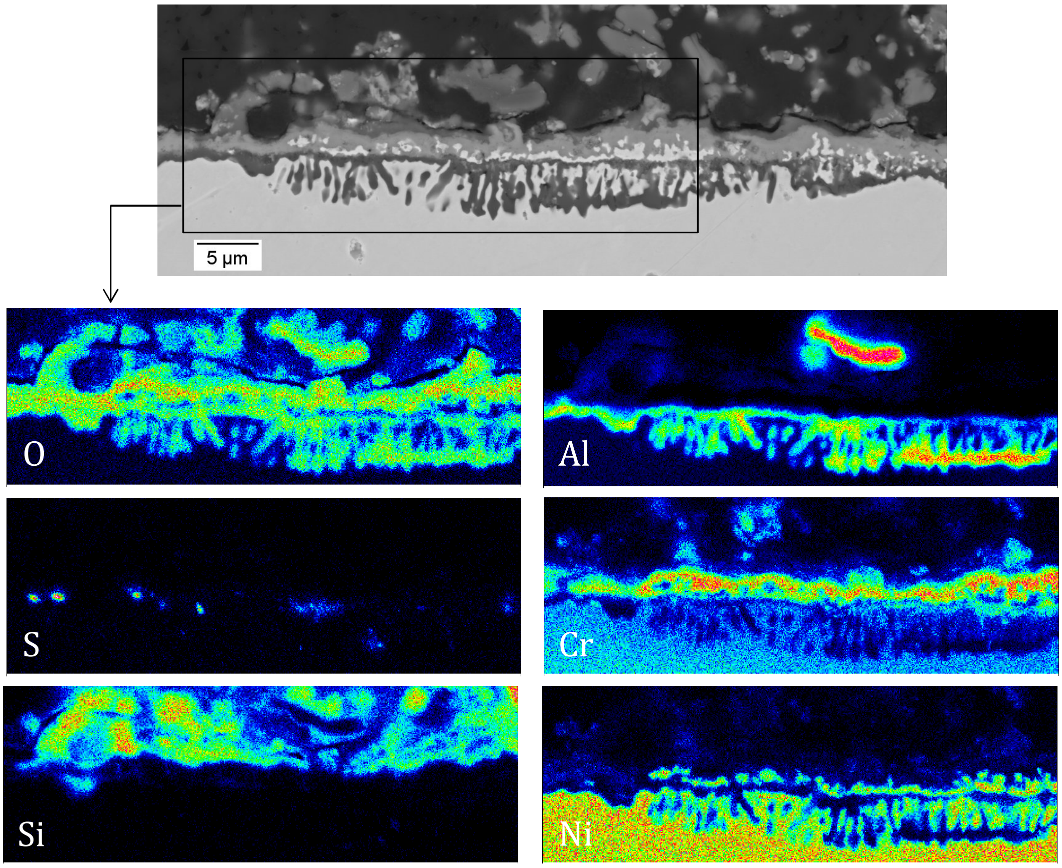

Figure 13: SEM view and WDS maps of corrosion product formed on Ni–30Co–27Cr–12Al-0.1Y after 1 h exposure to SiO_2–$20Al_2O_3$–33CaO–8MgO–$6Fe_2O_3$–$5Na_2SO_4$–$1K_2SO_4$ deposit in CO_2–$20H_2O$–$1.6O_2$ at 1100 °C. Repassivation starts as an Al_2O_3 sublayer forms at the base of the internal oxidation zone.

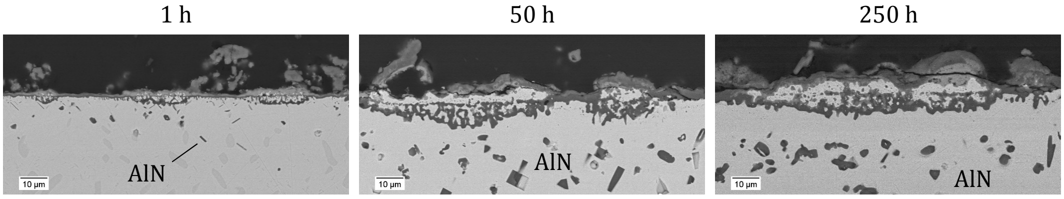

Figure 14: SEM cross-section of Ni–30Co–27Cr–12Al–0.1Y after 1, 50, and 250 h exposure to SiO_2–$20Al_2O_3$–33CaO–8MgO–$6Fe_2O_3$–$5Na_2SO_4$–$1K_2SO_4$ deposit in dry air at 1100 °C. The internal oxidation zone initially thickens as accelerated corrosion develops, until the alloy repassivates; Al nitrides are formed internally.

4 Discussion

4.1 Effects of alloy and gas compositions in the absence of a deposit

The influence of alloy microstructure on the oxide formed in the absence of a deposit was mostly visible on the β-rich alloys. The features observed here are consistent with descriptions of γ–β systems oxidation by previous investigators, e.g., Refs. [3–7]. After 5 min, the oxide grown on β still retained some transient θ-Al_2O_3, while that formed on γ was fully α-Al_2O_3 (Fig. 4). The faster $\theta \rightarrow \alpha$ transformation is usually attributed to the higher Cr content of the γ phase: the transient Cr_2O_3 it forms is thought to act as a template and to facilitate the nucleation of the isostructural α-Al_2O_3 [32,33]. The parabolic constant of θ is two orders of magnitude larger than that of α at 1100 °C [32,34], which is why the scale grown on β was thicker than that formed on γ after 20 min (Figs. 3 and 5). Yet, following the analysis of Brumm and Grabke [32], a delayed $\theta \rightarrow \alpha$ transformation also favors grain growth, which implies that the α-Al_2O_3 eventually present on β should have a coarser microstructure than that grown on γ. Since α-Al_2O_3 growth at this temperature is primarily by grain boundary diffusion, a larger-grained scale is expected to grow slower. Indeed, after 50 h, the oxide formed on β was significantly thinner than that formed on γ (Fig. 1e).

Although H_2O is known to enhance Al_2O_3 scale spallation [8–10], this did not affect the present isothermal exposures, as the 0.1 at. % Y provided good metal/oxide adherence even in wet atmospheres. Similarly, while H_2O may trigger internal oxidation of marginal Al_2O_3-formers [35], this was not the case here due to the relatively high Al and Cr concentrations. Chromia volatilization in wet atmospheres via Cr hydroxide formation is significant at 1100 °C [36]. While this is not the case of Al_2O_3 ($Al(OH)_3$ formation that is negligible below about 1300 °C [36]), $NiAl_2O_4$ was shown to sublime at significant rates in the presence of H_2O at 1100 °C [7]. In the present work, transient Cr_2O_3 and Cr-containing spinels formed on the γ phase, and their volatilization likely accounts for the reduction in scale thicknesses observed in H_2O-containing gases compared to dry air on the γ-rich alloys (Fig. 2). In the case of CO_2–$20H_2O$, the reduced p_{O_2} might also have contributed to produce thinner scales, since less transient oxides are typically observed at low p_{O_2} [37]. Finally, no effect of CO_2 was observed, which is consistent with observations made by other investigators after longer term testing in CO_2–H_2O [11,12].

4.2 Reaction mechanism of deposit-induced degradation

Exposure of the γ-rich alloys Ni–30Co–27Cr–12Al–0.1Y and Ni–30Co–30Cr–12Al–0.1Y to SiO_2–$25Al_2O_3$–$40CaO$–$10Na_2SO_4$ and SiO_2–$20Al_2O_3$–$33CaO$–$8MgO$–$6Fe_2O_3$–$5Na_2SO_4$–$1K_2SO_4$ deposits caused a transition to the internal oxidation of Al. The reaction products were equivalent regardless of gas composition. The same features were also observed after reaction of various MCrAlY compositions at 1100 °C with similar deposits, i.e., containing CaO and Na_2SO_4 [26]. We conclude that for a large part, the deposit-induced degradation of MCrAlY systems in S-free atmospheres at this temperature proceeds according to a common mechanism.

As mentioned in Section 3, the degradation was localized. The morphological continuity between intact Al_2O_3 scale, shallow intrusions and internal oxidation (Figs. 10 and 13) suggests that these were evolutionary steps of the same process. This process is shown schematically in Fig. 15a, and can be summarized as follows.

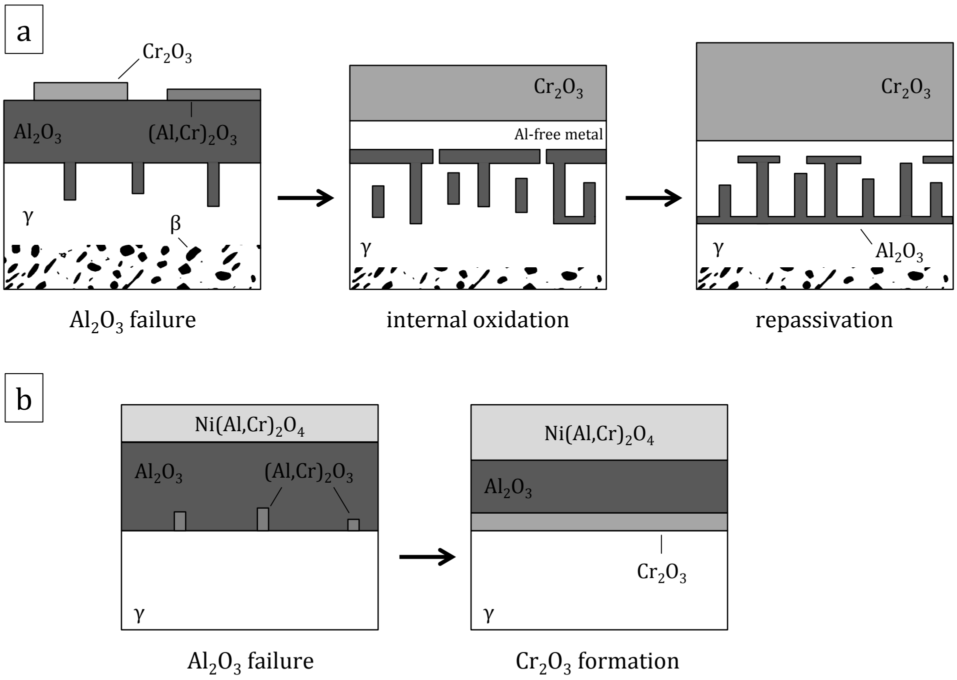

Figure 15: Schematic representation of transition from Al_2O_3 to Cr_2O_3 scaling in situations of (a) deposit-induced attack of Al_2O_3-former (present work) or oxidation of marginal Al_2O_3-former, and (b) "intrinsic chemical failure" due to complete exhaustion of Al in Al_2O_3-former.

As the initial Al_2O_3 lost its protective character, Al oxidized internally, first as intrusions in contact with the scale, then as discrete precipitates. The stress generated by internal oxidation is known to result in the extrusion of the alloy matrix, via Nabarro-Herring creep or dislocation pipe diffusion [38]. This produced a flow of Al-depleted, Cr-rich metal upward through discontinuities of the formerly protective scale. Oxidation of the extruded metal resulted in the growth of an external Cr_2O_3 scale. Thus, after the p_{O_2} at the metal surface rose following Al_2O_3 failure, it decreased back to the value set by the alloy/Cr_2O_3 equilibrium. This changed the balance of inward O and outward Al fluxes in favor of internal oxide growth against new nucleation, allowing a subsurface Al_2O_3 layer to develop at the reaction front by coalescence.

In examining the cause of the transition from external to internal Al oxidation, we note that the reaction morphology adopted after Al_2O_3 failure is, precisely, related to the "mode of failure," and ultimately to the conditions underlying Al_2O_3 stability as an external scale, which is dictated by kinetics. Due to the high thermodynamic stability of Al_2O_3, the Al activity required for Al–Al_2O_3 equilibrium is vanishingly small at practical p_{O_2} values. Any Al-containing alloy is thus expected to form Al_2O_3; yet it may fail to form it as an external scale if the outward Al flux is not sufficient to counter the inward O flux, in which case Al oxidizes internally instead [39, 40]. In accordance with the so-called gettering effect [41], if a Cr_2O_3 scale is present, the low p_{O_2} at the metal surface generates a limited O flux, and the Al concentration required for its external oxidation is also found to be very low. When an Al_2O_3 scale is formed, the Al flux still needs to match that required for the oxide to grow. Assuming parabolic oxidation kinetics and a constant Al diffusion coefficient in the alloy (D_{Al}), the minimum bulk Al fraction to sustain $\mathrm{Al_2O_3}$ growth is given by [42]:

$$N_{\mathrm{Al}}^{*} = F\left(\sqrt{\frac{1}{2}\frac{k_{\mathrm{c}}}{D_{\mathrm{Al}}}}\right) \tag{1}$$

where F is defined by $F(u) = \sqrt{\pi}u(1 - \operatorname{erf} u)\exp(u^2)$ and k_{c} is the parabolic constant for metal recession, defined by $d^2 = 2k_{\mathrm{c}}t$ with d the depth of the metal/oxide interface relative to the original alloy surface. For $N_{\mathrm{Al}} < N_{\mathrm{Al}}^{*}$, a Cr-rich alloy would form external $\mathrm{Cr_2O_3}$ and internal $\mathrm{Al_2O_3}$, as shown in Fig. 15a. This is the case of certain wrought austenitic Ni-base alloys with 2–5 at. % Al at temperatures above $\sim$ 850 °C [43–45]. For $N_{\mathrm{Al}} > N_{\mathrm{Al}}^{*}$, an $\mathrm{Al_2O_3}$ scale is kinetically stable but will eventually fail after the alloy Al reservoir is fully exhausted. When the depletion profiles generated on opposite sides of a specimen reach its center, the Al concentration at the metal/oxide interface starts to decrease, and the interfacial $p_{\mathrm{O_2}}$ rises until a $\mathrm{Cr_2O_3}$ sublayer forms, i.e., Cr reduces the $\mathrm{Al_2O_3}$. In this case, no internal oxidation of Al is possible, as its concentration profile is essentially flat, and $\mathrm{Al_2O_3}$ is not thermodynamically stable even below the surface. This “intrinsic chemical failure” [46], observed for long or high-temperature exposures of thin specimens [47–55], is represented schematically in Fig. 15b.

The alloys used here formed external $\mathrm{Al_2O_3}$ in the absence of a deposit ($N_{\mathrm{Al}} > N_{\mathrm{Al}}^{*}$), but developed a reaction morphology typical of alloys with sub-critical Al fraction ($N_{\mathrm{Al}} < N_{\mathrm{Al}}^{*}$) with an oxide–sulfate deposit present. The reaction of $\mathrm{Al_2O_3}$ with CaO to form Ca aluminates or its dissolution in molten $\mathrm{Na_2O}$–$\mathrm{SiO_2}$ each leads to an increased rate of Al consumption, potentially exceeding the Al flux available from the alloy and triggering internal oxidation. This amounts to a modification of the mass balance underlying Eq. (1), where k_{c} is replaced by a larger constant accounting for $\mathrm{Al_2O_3}$ consumption [25, 27]. Our study of various alloy and deposit compositions [26] showed that deposits containing CaO, $\mathrm{SiO_2}$, and $\mathrm{Na_2O}$ (as $\mathrm{Na_2SO_4}$) were susceptible to induce both modes of attack, solid-state reaction and liquid dissolution, and that $\mathrm{Al_2O_3}$ failure in γ-rich MCrAlY systems resulted from a combination of the two. While the assertion is justified, the present results indicate that $\mathrm{Al_2O_3}$ scales formed under the oxide–sulfate deposit were markedly different from those grown in the absence of a deposit, and suggest that additional factors played a role in their failure.

4.3 Deposit effects on $\mathrm{Al_2O_3}$ properties

The presence of the oxide–sulfate deposit affected the $\mathrm{Al_2O_3}$ scale in several ways. The possible causes and consequences of each aspect are discussed in the following.

$\mathrm{Al_2O_3}$ phase transition

The $\theta \rightarrow \alpha$ transition was delayed with the deposit present, compared to deposit-free exposures (see Fig. 4 for Ni–19Co–15Cr–24Al–0.1Y, equivalent results were obtained for Ni–30Co–30Cr–12Al–0.1Y in locations where an $\mathrm{Al_2O_3}$ scale was still present). The crystalline phases initially present in the deposit (α-quartz, α-$\mathrm{Al_2O_3}$, B1-CaO, B1-MgO, α-$\mathrm{Fe_2O_3}$) or formed by reaction with the scale (Ca and Mg aluminates) could in principle stabilize θ or α-Al_2O_3 via epitaxial relationships. Alternatively, the development of a reduced p_{O_2} beneath the deposit, in particular in the presence of molten phases (Na_2SO_4 or Na_2O–SiO_2), may also affect the transition. According to Nijdam et al. [6], a reduced p_{O_2} can either stabilize or suppress θ-Al_2O_3 on a NiCoCrAlY alloy at 1100 °C, depending on the p_{O_2} level and the heating procedure. Alvarado-Orozco et al. [56] reported that a p_{O_2} of 10^{-5} atm stabilized θ-Al_2O_3 on β–NiAl at 1000–1200 °C, compared to atmospheric pressure.

The mechanism of the $\theta \rightarrow \alpha$ transition is complex and system-dependent, and why a deposit would stabilize θ-Al_2O_3 remains unclear at present. However, a consequence is readily identified: as the parabolic constant of θ is two orders of magnitude larger than that of α at 1100 °C [32, 34], delaying the transition would maintain a higher rate of Al consumption, enhance Al depletion in the alloy and thereby favor internal oxidation. As discussed in Section 4.1, a delay is also expected to eventually produce a coarse-grained, slow-growing α-Al_2O_3.

Al_2O_3 microstructure

The microstructure of the Al_2O_3 grown beneath the deposit was significantly different from that of the scale grown in deposit-free conditions (compare Figs. 8 and 11). In particular, the Al_2O_3 grain size was much smaller with the deposit present, which is at variance with what could be expected from the delayed $\theta \rightarrow \alpha$ transition. This suggests that another aspect prevailed in determining the scale microstructure; specifically, the deposit either favored a faster nucleation or hindered grain growth or sintering, independently of the oxide crystal structure. Furthermore, the deposit caused the development of an interfacial gap, which was not observed in deposit-free conditions, and which indeed was much more extensive than the porosity usually observed in Al_2O_3 scales [57]. Both the smaller grain size and the interfacial gap can be interpreted as the result of a poisoning of interfacial reactions. As argued below, this is thought to be related to the presence of S in the system.

At a temperature where Al_2O_3 grows mainly by grain boundary diffusion, a smaller grain size is expected to yield a faster growth and enhanced Al consumption, adding to the delayed $\theta \rightarrow \alpha$ transition and further favoring internal oxidation. Exactly how much each contributed to Al_2O_3 failure is difficult to determine. Scale thicknesses measured after 20-min exposure with and without deposit, if converted to parabolic constants, both yield k_p values about 10 times larger than those obtained after 50-h exposure. This reflects the rapid evolution of Al_2O_3 microstructure in the first hours of oxidation, as discussed above, and as shown by thermogravimetric analysis of similar NiCoCrAlY compositions [25]. Such an evolution precludes a quantitative analysis of the effect of short-term deposit-induced microstructural changes on scaling kinetics, all the more so since these kinetics were also affected by the scale reaction with the deposit, independently of its microstructure.

Al_2O_3 permeability to secondary oxidants

The presence of the deposit rendered the Al_2O_3 scale permeable to secondary oxidants: S which was present as deposited sulfate, and N which was present as N_2 in air exposures. Chromium sulfide formation requires both an elevated S activity and a low p_{O_2} (high p_{O_2} stabilize sulfates rather than sulfides). Thus, the presence of such sulfides within the scale and at the metal/oxide interface (Fig. 11) indicates that the scale integrity was preserved to some extent, and that S permeated via small defects such as grain boundaries or sub-micron channels, rather than large cracks. Indeed, the scale appeared compact in the TEM. A high p_{S_2} could then be obtained by local equilibrium between incoming S-bearing molecules and the surrounding oxide, as discussed by Birks et al. [58, 59] in the case of Ni exposed to CO–CO_2–SO_2. Similar cases of attack by a secondary oxidant have been reported in various systems, e.g., carburization below Cr_2O_3 grown in CO–CO_2 [60–62]; yet the secondary oxidant was always present in the gas environment. On the other hand, Goebel and Pettit [63] showed that under a molten Na_2SO_4 deposit, O consumption due to oxidation could produce an elevated p_{S_2}. Recent work on Ni reaction at 700 °C [64] examined how this applied in S-containing and S-free atmospheres, with and without Na_2SO_4. Sulfidation was observed below Na_2SO_4, even in air. By analogy, we conclude that in the present case, a high p_{S_2} was generated at the oxide surface due to oxidation underneath the molten Na_2SO_4, and further amplified as S-bearing molecules traversed the scale, equilibrating with the surrounding p_{O_2}.

Alumina is generally believed to be a good barrier to secondary oxidants, more effective than Cr_2O_3 in particular [9], and reports of sulfidation below apparently compact Al_2O_3 scales are not frequent. Cases of Al_2O_3 permeation by S were reported on β-NiAl [65–68], where it led to the fast growth of porous Al_2O_3 nodules. Similar nodules were observed in cases where the S was present in the metal before oxidation [69, 70]; the widespread porosity was then attributed to SO_2 evolution. The present situation is different, as the scale remained thin and apparently compact above the gap separating it from the metal. Interfacial segregation of S was found in many systems [71–79] to reduce the oxide adherence. This was in part attributed to a reduction in the surface energy of interfacial pores [80–82] (these pores occur naturally due to vacancy injection, but remain much smaller in the absence of S). First-principles calculations also show that S weakens an intact Ni/Al_2O_3 bond [83–85].

In accordance with these findings, we conclude that S ingress through nano-sized defects of an initially compact scale, and its interfacial segregation, led to the observed gap; the latter might have been further stabilized by the establishment of an internal S_2–SO_2 mixture, which, like CO–CO_2 and H_2–H_2O mixtures in Fe oxide scales [86–89], would substantially increase the total pressure while a reduced p_{O_2} is maintained. A practical consequence of the peculiar microstructure observed in Fig. 11, and further indication that it was indeed related to S, is that all scales formed under Na_2SO_4-containing deposits showed significant spallation.

Furthermore, the fact that the deposit also made Al_2O_3 scales permeable to N, even in locations where they were apparently intact and the transition to internal oxidation had not started, leads to the conclusion that the scale microstructural changes were accompanied by a loss of protective properties. Specifically, despite the scale compact appearance in the TEM, the density of nano-scale defects capable of transmitting secondary oxidants such as N_2 or SO_2 must have been greatly increased. The grain boundary density increased simply due to the smaller grain size, but this would hardly account for the increased permeability. Instead, the grain boundary properties must have themselves been affected.

Finally, in terms of scale stability, a common effect of the reaction with secondary oxidants is that it reduces the availability of the oxide-forming element, which may lead to non-selective oxidation [60]. Here sulfides were either Cr-rich (Fig. 11) or mixed Cr–Ni (Fig. 12), which did not affect the Al supply. Internal nitrides were Al-rich, but no significant effect on the extent of internal oxidation was observed.

4.4 Effects of alloy and gas compositions on deposit-induced attack

Both the delayed $\theta \rightarrow \alpha$ transition and the smaller grain size of the Al_2O_3 grown with the deposit present are expected to accelerate Al consumption and favor internal oxidation. This would affect γ-rich alloys more than β-rich alloys, because the former have a smaller Al reservoir to start with. Furthermore, the $\theta \rightarrow \alpha$ transition is more rapid on γ than on β in the absence of a deposit (Fig. 4), which makes γ-rich alloys all the more susceptible to the delaying action of the deposit.

Alloys with larger Cr concentrations tend to sustain more degradation by CaO-rich deposits, because of the rapid reaction of transient Cr-rich oxide with CaO to form a liquid Ca chromate [25]. While the specifics of the reaction mechanism are not fully understood at present, larger Cr concentrations were also found to locally accelerate the initiation of Al_2O_3 dissolution in molten Na_2O–SiO_2, promoting Al_2O_3 failure [26, 27]. Therefore, the fact that the γ-rich alloys used here had high Cr levels and formed relatively large amounts of Cr-rich transient oxide, compared to the Cr-lean β-rich alloy (see Section 3.1), presumably contributed to the non-selective oxidation exhibited under the deposit. Accordingly, the reduced transient Cr oxidation observed in deposit-free conditions in wet atmospheres, compared to dry air, and due to H_2O-mediated volatilization (see Section 4.1), could have mitigated the deleterious effect of the large Cr levels. This was in fact not the case, as results observed with a deposit present in wet atmospheres and dry air were equivalent. A possible reason for this is that the deposit may have affected the gas flow accessible to the specimen surfaces, hampering volatilization; in addition, the reaction of Cr-rich oxide with CaO or Na_2O–SiO_2 in the very early stage of the exposure may have been so fast that it was insensitive to volatilization.

Finally, the fact that after Al_2O_3 breakdown, an external Cr_2O_3 layer formed and remained stable, favoring repassivation (Section 4.2), may seem to be in contradiction with the tendency of Cr_2O_3 to react very rapidly with CaO in the transient stage [25]. Molten Ca chromate was observed to form under mixed deposits despite the fact that adding Al_2O_3 or SiO_2 reduced the CaO activity, compared to a pure CaO deposit [26]. The apparent difference in Cr_2O_3 reactivity between the transient stage and steady state is likely due to a CaO depletion in the regions of the deposit closest to the specimen surface. Experiments where some fresh deposit is periodically re-applied would be useful to study the stability of the external Cr_2O_3 layer in more realistic conditions.

5 Conclusions

The deposit-induced accelerated degradation of γ-rich NiCoCrAlY alloys involved, in its early stage, the breakdown of an initially formed Al_2O_3 scale, the development of Al_2O_3 intrusions and internal precipitates, and the establishment of an external Cr_2O_3 layer. This was followed by a repassivation stage, where a new Al_2O_3 layer formed at the internal oxidation front. This morphological evolution is in part similar to that observed on more dilute NiCrAl-base alloys; its occurrence on compositions which form Al_2O_3 scales in the absence of a deposit reflects the "mode of failure" associated with the deposit-induced attack: the Al_2O_3 scale fails because of its reaction with the deposit, but once the alloy is isolated from the deposit by a Cr_2O_3 layer, it returns to forming a continuous Al_2O_3 layer. The protecting role of the external Cr_2O_3 may, however, be challenged if fresh CaO-rich deposit is re-applied, because of the formation of liquid Ca chromate.

Detailed analysis of the reaction products formed during the early stage of the reaction, before the transition from external to internal Al_2O_3 growth, showed that in addition to reacting in the solid state (to form Ca aluminates) or dissolving in a liquid phase (molten Na_2O–SiO_2), the Al_2O_3 scale microstructure was affected by the deposit. Compared to deposit-free conditions, the $\theta \rightarrow \alpha$ transformation was delayed, the scale grain size was reduced, both factors further increasing Al consumption and favoring internal oxidation. In addition, the scale adherence was reduced, to an extent where a nearly continuous gap developed at the metal/oxide interface. Sulfur ingress through nano-sized defects of the initially compact scale, and its interfacial segregation, were concluded to be the cause of both the interfacial gap and the reduced grain size. The observation that scales grown under the deposit were permeable to N also led to the conclusion that the modified microstructure involved a loss of protective properties, specifically, that the grain boundary ability to block molecules of secondary oxidants was reduced.

Sulfide formation in the alloys exposed to the deposit showed that Na_2SO_4 allowed sulfidizing conditions to establish, even in S-free atmospheres. Sulfidation and nitridation were consequences of the deposit-induced degradation, but neither was found in itself to significantly affect the corrosion resistance. Similarly, no interaction between the other gas constituents (CO_2, H_2O) and the deposits was observed.

Acknowledgements

This work was supported by the Department of Energy through the University Turbine Systems Research (UTSR) Program run by the National Energy Technology Laboratory, award number DE–FE0007271, Seth Lawson, Project Manager. The authors thank Maryam Zahiri Azar and Arthur Heuer (Case Western Reserve University), as well as Susheng Tan (University of Pittsburgh), for the FIB and TEM work.

References

[1] R. C. Reed, *The Superalloys: Fundamentals and Applications*. Cambridge University Press (2006).

[2] S. Bose, *High Temperature Coatings*. Burlington: Butterworth-Heinemann (2007).

[3] D. Clemens, V. Vosberg, W. Hobbs, U. Breuer, W. J. Quadakkers and H. Nickel, TEM and SNMS studies of protective alumina scales on NiCrAlY-alloys, Fresenius Journal of Analytical Chemistry 355 (1996) pp. 703–706. doi: 10.1007/s0021663550703.

[4] C. Mennicke, D. Mumm and D. Clarke, Transient phase evolution during oxidation of a two-phase NiCoCrAlY bond coat, Zeitschrift für Metallkunde 90 (1999) pp. 1079–1084.

[5] C. G. Levi, E. Sommer, S. G. Terry, A. Catanoiu and M. Rühle, Alumina grown during deposition of thermal barrier coatings on NiCrAlY, Journal of the American Ceramic Society 86 (2003) pp. 676–85. doi: 10.1111/j.1151-2916.2003.tb03357.x.

[6] T. J. Nijdam, L. P. H. Jeurgens, J. H. Chen and W. G. Sloof, On the microstructure of the initial oxide grown by controlled annealing and oxidation on a NiCoCrAlY bond coating, Oxidation of Metals 64 (2005) pp. 355–377. doi: 10.1007/s11085-005-8532-6.

[7] M. H. Sullivan and D. R. Mumm, Vapor-phase-mediated phenomena associated with high temperature, high water content oxidation of MCrAlX bond coats, Oxidation of Metals 82 (2014) pp. 1–20. doi: 10.1007/s11085-014-9473-8.

[8] N. Birks, G. H. Meier and F. S. Pettit, *Introduction to the High Temperature Oxidation of Metals.* Cambridge University Press 2nd ed. (2006).

[9] D. J. Young, *High Temperature Oxidation and Corrosion of Metals.* Elsevier Corrosion Series Elsevier (2008).

[10] S. R. J. Saunders, M. Monteiro and F. Rizzo, The oxidation behaviour of metals and alloys at high temperatures in atmospheres containing water vapour: a review, Progress in Materials Science 53 (2008) pp. 775–837. doi: 10.1016/j.pmatsci.2007.11.001.

[11] S. Dryepondt, A. Rouaix-Vande Put and B. A. Pint, Effect of H_2O and CO_2 on the oxidation behavior and durability at high temperature of ODS–FeCrAl, Oxidation of Metals 79 (2013) pp. 627–638. doi: 10.1007/s11085-013-9382-2.

[12] M. Lance, K. Unocic, J. Haynes and B. Pint, The effect of cycle frequency, H_2O and CO_2 on TBC lifetime with NiCoCrAlYHfSi bond coatings, Surface and Coatings Technology 260 (2014) pp. 107–112. doi: 10.1016/j.surfcoat.2014.08.082.

[13] J. A. Goebel, F. S. Pettit and G. W. Goward, Mechanisms for hot corrosion of nickel-base alloys, Metallurgical Transactions 4 (1973) pp. 261–278. doi: 10.1007/bf02649626.

[14] J. Stringer, Hot corrosion of high-temperature alloys, Annual Review of Materials Science 7 (1977) pp. 477–509. doi: 10.1146/annurev.ms.07.080177.002401.

[15] R. A. Rapp, Chemistry and electrochemistry of the hot corrosion of metals, Corrosion 42 (1986) pp. 568–577. doi: 10.5006/1.3583026.

[16] G. W. Goward, Low-temperature hot corrosion in gas-turbines: a review of causes and coatings therefor, Journal of Engineering for Gas Turbines and Power 108 (1986) pp. 421–425. doi: 10.1115/1.3239921.

[17] N. Birks, G. H. Meier and F. S. Pettit, *Chapter 8 in Introduction to the High Temperature Oxidation of Metals.* Cambridge University Press 2nd ed. (2006).

[18] F. Pettit, Hot corrosion of metals and alloys, Oxidation of Metals 76 (2011) pp. 1–21. doi: 10.1007/s11085-011-9254-6.

[19] C. G. Levi, J. W. Hutchinson, M.-H. Vidal-Setif and C. A. Johnson, Environmental degradation of thermal-barrier coatings by molten deposits, MRS Bulletin 37 (2012) pp. 932–941. doi: 10.1557/mrs.2012.230.

[20] J. P. Bons, J. Crosby, J. E. Wammack, B. I. Bentley and T. H. Fletcher, High-pressure turbine deposition in land-based gas turbines from various synfuels, Journal of Engineering for Gas Turbines and Power 129 (2005) pp. 135–143. doi: 10.1115/1.2181181.

[21] P. Wu, G. Eriksson and A. D. Pelton, Optimization of the thermodynamic properties and phase diagrams of the Na_2O-SiO_2 and K_2O-SiO_2 systems, Journal of the American Ceramic Society 76 (1993) pp. 2059–2064. doi: 10.1111/j.1151-2916.1993.tb08333.x.

[22] E. Levin, C. Robbins and H. McMurdie, *Phase diagrams for ceramists* vol. 1. The American Ceramic Society, Columbus, OH (1964).

[23] A. Kaiser, B. Sommer and E. Woermann, The system CaO–$CaCr_2O_4$–$CaAl_2O_4$ in air and under mildly reducing conditions, Journal of the American Ceramic Society 75 (1992) pp. 1463–1471. doi: 10.1111/j.1151-2916.1992.tb04211.x.

[24] K. T. Chiang, G. H. Meier and R. A. Perkins, The effects of deposits of CaO, $CaSO_4$, and MgO on the oxidation of several Cr_2O_3-forming and Al_2O_3-forming alloys, Journal of Materials for Energy Systems 6 (1984) pp. 71–86. doi: 10.1007/BF02833417.

[25] T. Gheno, G. H. Meier and B. Gleeson, High temperature reaction of MCrAlY coating compositions with CaO deposits, Oxidation of Metals 84 (2015) pp. 185–209. doi: 10.1007/s11085-015-9550-7.

[26] T. Gheno and B. Gleeson, Modes of deposit-induced accelerated attack of MCrAlY systems at 1100 °C, Oxidation of Metals 87 (2017) pp. 249–270. doi: 10.1007/s11085-016-9669-1.

[27] T. Gheno and B. Gleeson, Kinetics of Al_2O_3-scale growth by oxidation and dissolution in molten silicate, Oxidation of Metals 87 (2017) pp. 527–539. doi: 10.1007/s11085-016-9686-0.

[28] Materials Preparation Center, Ames Laboratory, US DOE Basic Energy Sciences, Ames, IA, USA, available from: `www.ameslab.gov/mpc`.

[29] C. A. Schneider, W. S. Rasband and K. W. Eliceiri, NIH image to ImageJ: 25 years of image analysis, Nature Methods 9 (2012) pp. 671–675. doi: 10.1038/nmeth.2089.

[30] V. K. Tolpygo and D. R. Clarke, Microstructural study of the theta-alpha transformation in alumina scales formed on nickel-aluminides, Materials at High Temperatures 17 (2000) pp. 59–70. doi: 10.1179/mht.2000.011.

[31] I. Barin, *Thermochemical Data of Pure Substances.* VCH second ed. (1993).

[32] M. W. Brumm and H. J. Grabke, The oxidation behavior of NiAl. 1. Phase-transformations in the alumina scale during oxidation of NiAl and NiAl–Cr alloys, Corrosion Science 33 (1992) pp. 1677–1690. doi: 10.1016/0010-938x(92)90002-k.

[33] Y. Kitajima, S. Hayashi, T. Nishimoto, T. Narita and S. Ukai, Rapid formation of α-Al_2O_3 scale on an Fe–Al alloy by pure-metal coatings at 900 °C, Oxidation of Metals 73 (2010) pp. 375–388. doi: 10.1007/s11085-009-9184-8.

[34] G. C. Rybicki and J. L. Smialek, Effect of the θ–α-Al_2O_3 transformation on the oxidation behavior of β-NiAl+Zr, Oxidation of Metals 31 (1989) pp. 275–304. doi: 10.1007/bf00846690.

[35] W. Zhao and B. Gleeson, Assessment of the detrimental effects of steam on Al_2O_3-scale establishment, Oxidation of Metals 83 (2015) pp. 607–627. doi: 10.1007/s11085-015-9541-8.

[36] E. J. Opila, N. S. Jacobson, D. L. Myers and E. H. Copland, Predicting oxide stability in high-temperature water vapor, JOM 58 (2006) pp. 22–28. doi: 10.1007/s11837-006-0063-3.

[37] T. Nijdam, L. Jeurgens and W. Sloof, Promoting exclusive α-Al_2O_3 growth upon high-temperature oxidation of NiCrAl alloys: experiment versus model predictions, Acta Materialia 53 (2005) pp. 1643–1653. doi: 10.1016/j.actamat.2004.12.014.

[38] H. Yi, S. Guan, W. Smeltzer and A. Petric, Internal oxidation of NiAl and NiAlSi alloys at the dissociation pressure of NiO, Acta Metallurgica et Materialia 42 (1994) pp. 981–990. doi: 10.1016/0956-7151(94)90292-5.

[39] C. Wagner, Reaktionstypen bei der Oxydation von Legierungen, Zeitschrift für Elektrochemie 63 (1959) pp. 772–790. doi: 10.1002/bbpc.19590630713.

[40] R. Rapp, Kinetics, microstructures and mechanism of internal oxidation - its effect and prevention in high temperature alloy oxidation, Corrosion 21 (1965) pp. 382–401. doi: 10.5006/0010-9312-21.12.382.

[41] C. Wagner, Passivity and inhibition during the oxidation of metals at elevated temperatures, Corrosion Science 5 (1965) pp. 751–764. doi: 10.1016/S0010-938X(65)80003-8.

[42] C. Wagner, Theoretical analysis of the diffusion processes determining the oxidation rate of alloys, Journal of the Electrochemical Society 99 (1952) pp. 369–380. doi: 10.1149/1.2779605.

[43] G. Gulsoy and G. S. Was, Mechanism of internal oxidation of alloy 617 in He–CO–CO_2 environments at 1123 K (850 °C), Metallurgical and Materials Transactions A 46 (2015) pp. 525–535. doi: 10.1007/s11661-014-2629-y.

[44] M. Schiek, L. Niewolak, W. Nowak, G. H. Meier, R. Vaßen and W. J. Quadakkers, Scale formation of alloy 602 CA during isothermal oxidation at 800–1100 °C in different types of water vapor containing atmospheres, Oxidation of Metals 84 (2015) pp. 661–694. doi: 10.1007/s11085-015-9595-7.

[45] A. Chyrkin, W. G. Sloof, R. Pillai, T. Galiullin, D. Grüner, L. Singheiser and W. J. Quadakkers, Modelling compositional changes in nickel base alloy 602 CA during high temperature oxidation, Materials at High Temperatures 32 (2015) pp. 102–112. doi: 10.1179/0960340914z.00000000082.

[46] H. E. Evans, A. T. Donaldson and T. C. Gilmour, Mechanisms of breakaway oxidation and application to a chromia-forming steel, Oxidation of Metals 52 (1999) pp. 379–402. doi: 10.1023/A:1018855914737.

[47] W. Quadakkers and M. Bennett, Oxidation induced lifetime limits of thin walled, iron based, alumina forming, oxide dispersion strengthened alloy components, Materials Science and Technology 10 (1994) pp. 126–131. doi: 10.1179/mst.1994.10.2.126.

[48] I. Wright, B. Pint, C. Simpson and P. Tortorelli, High-temperature oxidation life characteristics of ODS–Fe_3Al, Materials science forum 251–254 (1997) pp. 195–202. doi: 10.4028/www.scientific.net/MSF.251-254.195.

[49] F. H. Stott and N. Hiramatsu, Breakdown of protective scales during the oxidation of thin foils of Fe–20Cr–5Al alloys at high temperatures, Materials at High Temperatures 17 (2000) pp. 93–99. doi: 10.1179/mht.2000.015.

[50] H. Al-Badairy, G. J. Tatlock and M. J. Bennett, A comparison of breakaway oxidation in wedge-shaped and parallel sided coupons of FeCrAl alloys, Materials at High Temperatures 17 (2000) pp. 101–107. doi: 10.1179/mht.2000.016.

[51] I. G. Wright, R. Peraldi and B. A. Pint, Influence of aluminum depletion effects on the calculation of the oxidation lifetimes of FeCrAl alloys, Materials Science Forum 461–464 (2004) pp. 579–590. doi: 10.4028/www.scientific.net/MSF.461-464.579.

[52] G. J. Tatlock, H. Al-Badairy, M. J. Bennett, R. Newton, J. R. Nicholls and A. Galerie, Air oxidation of commercial FeCrAlRE alloy foils between 800 and 950 °C, Materials Science and Technology 21 (2005) pp. 893–900. doi: 10.1179/174328405X46123.

[53] G. Strehl, P. Beaven, B. Lesage and G. Borchardt, Two calculations concerning the critical aluminium content in Fe20Cr5Al alloys, Materials and Corrosion 56 (2005) pp. 778–784. doi: 10.1002/maco.200503878.

[54] D. J. Young, A. Chyrkin, J. He, D. Grüner and W. J. Quadakkers, Slow transition from protective to breakaway oxidation of Haynes 214 foil at high temperature, Oxidation of Metals 79 (2013) pp. 405–427. doi: 10.1007/s11085-013-9364-4.

[55] A. Chyrkin, N. Mortazavi, M. Halvarsson, D. Grüner and W. Quadakkers, Effect of thermal cycling on protective properties of alumina scale grown on thin Haynes 214 foil, Corrosion Science 98 (2015) pp. 688–698. doi: 10.1016/j.corsci.2015.06.020.

[56] J. M. Alvarado-Orozco, R. Morales-Estrella, M. S. Boldrick, G. Trapaga-Martinez, B. Gleeson and J. Munoz-Saldana, Kinetic study of the competitive growth between θ-Al_2O_3 and α-Al_2O_3 during the early stages of oxidation of β-(Ni,Pt)Al bond coat systems: Effects of low oxygen partial pressure and temperature, Metallurgical and Materials Transactions A 46 (2015) pp. 726–738. doi: 10.1007/s11661-014-2669-3.

[57] B. A. Pint, On the formation of interfacial and internal voids in α-Al_2O_3 scales, Oxidation of Metals 48 (1997) pp. 303–328. doi: 10.1007/BF01670505.

[58] N. Birks, Corrosion mechanisms of metals and alloys in multicomponent oxidative environments, in *Proceedings of the symposium on properties of high temperature alloys with emphasis on environmental effects (Electrochemical Society, Las Vegas, 1976)* (Z. A. Foroulis and F. S. Pettit, eds.) p. 215.

[59] M. C. Pope and N. Birks, The penetration by sulfur of NiO scales growing on nickel, Oxidation of Metals 12 (1978) pp. 173–181. doi: 10.1007/BF00740258.

[60] C. S. Giggins and F. S. Pettit, Corrosion of metals and alloys in mixed gas environments at elevated temperatures, Oxidation of Metals 14 (1980) pp. 363–413. doi: 10.1007/BF00603609.

[61] X. G. Zheng and D. J. Young, High-temperature corrosion of Cr_2O_3-forming alloys in CO–CO_2–N_2 atmospheres, Oxidation of Metals 42 (1994) pp. 163–190. doi: 10.1007/BF01052021.

[62] T. Gheno, D. Monceau, J. Zhang and D. J. Young, Carburisation of ferritic Fe–Cr alloys by low carbon activity gases, Corrosion Science 53 (2011) pp. 2767–2777. doi: 10.1016/j.corsci.2011.05.013.

[63] J. A. Goebel and F. S. Pettit, Na_2SO_4-induced accelerated oxidation (hot corrosion) of nickel, Metallurgical Transactions 1 (1970) pp. 1943–1954. doi: 10.1007/BF02642794.

[64] T. Gheno and B. Gleeson, On the hot corrosion of nickel at 700 °C, Oxidation of Metals 84 (2015) pp. 567–584. doi: 10.1007/s11085-015-9588-6.

[65] M. Brumm, H. Grabke and B. Wagemann, The oxidation of NiAl. 3. Internal and intergranular oxidation, Corrosion Science 36 (1994) pp. 37–53. doi: 10.1016/0010-938X(94)90107-4.

[66] B. Schramm and W. Auer, Sulfidation behaviour of nickel aluminides, Materials and Corrosion 47 (1996) pp. 678–684. doi: 10.1002/maco.19960471204.

[67] H. J. Grabke and G. H. Meier, Accelerated oxidation, internal oxidation, intergranular oxidation, and pesting of intermetallic compounds, Oxidation of Metals 44 (1995) pp. 147–176. doi: 10.1007/BF01046726.

[68] T. Gheno, M. Zahiri Azar, A. H. Heuer and B. Gleeson, Reaction morphologies developed by nickel aluminides in type II hot corrosion conditions: The effect of chromium, Corrosion Science 101 (2015) pp. 32–46. doi: 10.1016/j.corsci.2015.08.029.

[69] J. A. Goebel and F. S. Pettit, Influence of sulfides on oxidation behavior of nickel-base alloys, Metallurgical Transactions 1 (1970) pp. 3421–3429. doi: 10.1007/BF03037874.

[70] J. L. Smialek, Non-protective alumina growth in sulfur-doped NiAl(Zr), Materials at High Temperatures 17 (2000) pp. 71–77. doi: 10.1179/mht.2000.012.

[71] A. W. Funkenbusch, J. G. Smeggil and N. S. Bornstein, Reactive element-sulfur interaction and oxide scale adherence, Metallurgical Transactions A 16 (1985) pp. 1164–1166. doi: 10.1007/BF02811687.

[72] J. G. Smeggil, A. W. Funkenbusch and N. S. Bornstein, A relationship between indigenous impurity elements and protective oxide scale adherence characteristics, Metallurgical Transactions A 17 (1986) pp. 923–932. doi: 10.1007/bf02661258.

[73] J. L. Smialek, Adherent Al_2O_3 scales formed on undoped NiCrAl alloys, Metallurgical Transactions A 18 (1987) pp. 164–167. doi: 10.1007/BF02646237.

[74] P. Y. Hou and J. Stringer, Oxide scale adhesion and impurity segregation at the scale/metal interface, Oxidation of Metals 38 (1992) pp. 323–345. doi: 10.1007/BF00665658.

[75] J. L. Smialek, D. T. Jayne, J. C. Schaeffer and W. H. Murphy, Effects of hydrogen annealing, sulfur segregation and diffusion on the cyclic oxidation resistance of superalloys - a review, Thin Solid Films 253 (1994) pp. 285–292. doi: 10.1016/0040-6090(94)90335-2.

[76] J. Smialek, Maintaining adhesion of protective Al_2O_3 scales, JOM 52 (2000) pp. 22–25. doi: 10.1007/s11837-000-0110-4.

[77] P. Hou and J. L. Smialek, The effect of H_2-anneal on the adhesion of Al_2O_3 scales on a Fe_3Al-based alloy, Materials at High Temperatures 17 (2000) pp. 79–85. doi: 10.1179/mht.2000.013.

[78] J. L. Smialek and B. A. Pint, Optimizing scale adhesion on single crystal superalloys, Materials science forum 369–372 (2001) pp. 459–466. doi: 10.4028/www.scientific.net/MSF.369-372.459.

[79] P. Y. Hou, T. Izumi and B. Gleeson, Sulfur segregation at Al_2O_3/γ-Ni + γ'-Ni_3Al interfaces: Effects of Pt, Cr and Hf additions, Oxidation of Metals 72 (2009) pp. 109–124. doi: 10.1007/s11085-009-9149-y.

[80] H. Grabke, D. Wiemer and H. Viefhaus, Segregation of sulfur during growth of oxide scales, Applied Surface Science 47 (1991) pp. 243–250. doi: 10.1016/0169-4332(91)90038-L.

[81] H. J. Grabke, G. Kurbatov and H. J. Schmutzler, Segregation beneath oxide scales, Oxidation of Metals 43 (1995) pp. 97–114. doi: 10.1007/BF01046749.

[82] P. Hou and K. Priimak, Interfacial segregation, pore formation, and scale adhesion on NiAl alloys, Oxidation of Metals 63 (2005) pp. 113–130. doi: 10.1007/s11085-005-1954-3.

[83] S. Hong, A. B. Anderson and J. L. Smialek, Sulfur at nickel-alumina interfaces: Molecular orbital theory, Surface Science 230 (1990) pp. 175–183. doi: 10.1016/0039-6028(90)90025-4.

[84] W. Zhang, J. R. Smith, X.-G. Wang and A. G. Evans, Influence of sulfur on the adhesion of the nickel/alumina interface, Physical Review B 67 (2003) p. 245414. doi: 10.1103/PhysRevB.67.245414.

[85] Y. Jiang and J. R. Smith, Pt effects in γ-Ni(Al)/α-Al_2O_3 adhesion, Journal of Materials Science 44 (2009) p. 1734. doi: 10.1007/s10853-008-3084-1.

[86] C. T. Fujii and R. A. Meussner, The mechanism of the high-temperature oxidation of iron-chromium alloys in water vapor, Journal of the Electrochemical Society 111 (1964) pp. 1215–1221. doi: 10.1149/1.2425963.

[87] A. Rahmel and J. Tobolski, Einfluss von Wasserdampf und Kohlendioxyd auf die Oxydation von Eisen in Sauerstoff bei Hohen Temperaturen, Corrosion Science 5 (1965) pp. 333–346. doi: 10.1016/S0010-938X(65)90500-7.

[88] C. T. Fujii and R. A. Meussner, Carburization of Fe–Cr alloys during oxidation in dry carbon dioxide, Journal of the Electrochemical Society 114 (1967) pp. 435–442. doi: 10.1149/1.2426622.

[89] J. Ehlers, D. Young, E. Smaardijk, A. Tyagi, H. Penkalla, L. Singheiser and W. Quadakkers, Enhanced oxidation of the 9%cr steel P91 in water vapour containing environments, Corrosion Science 48 (2006) pp. 3428–3454. doi:10.1016/j.corsci.2006.02.002.